

Excitonic Stark effect in MoS₂ monolayers

Benedikt Scharf,^{1,2,*} Tobias Frank,³ Martin Gmitra,³ Jaroslav Fabian,³ Igor Žutić,^{1,†} and Vasili Perebeinos^{2,‡}

¹*Department of Physics, University at Buffalo, State University of New York, Buffalo, NY 14260, USA*

²*Skolkovo Institute of Science and Technology, 100 Novaya Street, Skolkovo, Moscow Region 143025, Russia*

³*Institute for Theoretical Physics, University of Regensburg, 93040 Regensburg, Germany*

(Dated: November 26, 2018)

We theoretically investigate excitons in MoS₂ monolayers in an applied in-plane electric field. Tight-binding and Bethe-Salpeter equation calculations predict a quadratic Stark shift, of the order of a few meV for fields of 10 V/μm, in the linear absorption spectra. The spectral weight of the main exciton peaks decreases by a few percent with an increasing electric field due to the exciton field ionization into free carriers as reflected in the exciton wave functions. Subpicosecond exciton decay lifetimes at fields of a few tens of V/μm could be utilized in solar energy harvesting and photodetection. We find simple scaling relations of the exciton binding, radius, and oscillator strength with the dielectric environment and an electric field, which provides a path to engineering the MoS₂ electro-optical response.

PACS numbers: 78.67.-n, 71.35.-y, 78.20.Jq

Keywords: excitons, Stark effect, transition metal dichalcogenides

I. INTRODUCTION

In the past decade, atomically thin two-dimensional (2D) layers have emerged as a class of very versatile materials with highly tunable electronic and optical properties. Among these materials, a finite direct band gap makes monolayers (MLs) of MoS₂ and other transition metal dichalcogenides^{1–4} (TMDs) attractive candidates for possible applications in nanoscale electronics, optoelectronics, and energy harvesting.^{5–14}

Due to inversion symmetry breaking, combined with strong spin-orbit coupling (SOC), these materials show several peculiar properties such as valley-dependent optical selection rules that allow for an efficient control of the spin- and valley-degrees of freedom by optical helicity,^{15–18} the valley Hall¹⁹ and valley Zeeman^{20,21} effects, as well as strong magneto-²² and photoluminescence^{2,23} with a quantum yield that can exceed 95%.²⁴ In the context of spintronics,²⁵ based on the large difference between the spin relaxation times of electrons and holes in TMDs,^{26,27} MoS₂ has been predicted as a desirable active region for spin-lasers,²⁸ while hybrid structures of graphene on TMDs have been proposed as a platform for optospintronics.²⁹

One of the most intriguing aspects of ML TMDs is that the interplay of their 2D character and enhanced Coulomb interactions leads to pronounced many-body effects that also dominate their optical properties. Strong excitonic effects with binding energies of several hundreds of meV, orders of magnitude larger than in conventional 3D semiconductors, are predicted in TMDs.^{30–41} Due to the peculiar 2D screening these excitons are, moreover, expected to deviate from a simple hydrogen model. These predictions, large binding energies and a nonhydrogenic Rydberg series, have recently been confirmed experimentally.^{42–50} Likewise, the binding energies of trions (charged excitons) are also much larger in TMDs than in conventional semiconductors, of the order of sev-

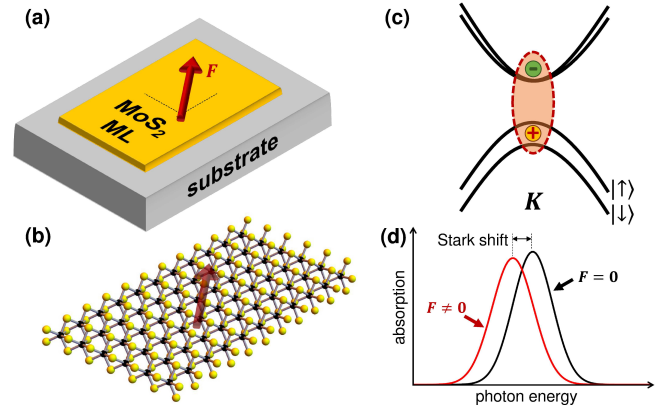


FIG. 1. (Color online) (a) Schematic setup of the system investigated, (b) MoS₂ monolayer (ML), (c) formation of the lowest-energy exciton, the so-called A exciton, at the K point in a MoS₂ ML, and (d) manifestation of the Stark effect on an exciton absorption peak if an electric field \mathbf{F} is applied.

eral tens of meV.^{33,38,51–53} Indirect excitons in TMD-based van der Waals heterostructures similarly possess large binding energies and can be controlled by an electrostatic gate voltage.^{54,55}

In the present work, we study ML MoS₂ as the prototype material for ML TMDs and how excitons and the optical absorption in this system are affected by a constant in-plane electric field [Figs. 1 (a, b)]. Almost 60 years ago, Franz and Keldysh predicted a modulation of the band-edge absorption due to the electric field in bulk semiconductors.⁵⁶ If the effect of the Coulomb interaction between electrons and holes and, in consequence, excitons are taken into account [Fig. 1 (c)], an excitonic Stark effect arises [Fig. 1 (d)]: Similar to the hydrogen atom, there is a quadratic energy shift of the non-degenerate lowest energy exciton in the applied electric field.

However, this effect is not easily observed in bulk semi-

conductors due to the low exciton binding energies exhibited in these systems. In contrast, as a consequence of their large exciton binding energies, TMDs enable probing an excitonic Stark effect, similar to quantum well structures,⁵⁷ carbon nanotubes,⁵⁸ or black phosphorus.⁵⁹ In fact, the Stark effect due to an out-of-plane electric field has recently been observed in mono- and few-layer TMDs,^{60,61} while an a.c. optical Stark effect has been demonstrated in WSe₂ and WS₂, important for quantum information applications with TMDs.^{62,63}

We predict a quadratic Stark shift with the in-plane field, which depends sensitively on the dielectric environment and is of the order of several meV or even larger for fields of a few tens of V/ μm . Moreover, we provide the corresponding scaling laws for experimentally observable quantities such as the Stark shift and the loss of oscillator strength, demonstrating a tunable electro-optical response in MoS₂. While the focus of this work is on the linear absorption and thus on bright *s*-like excitons, we also predict a nonlinear Stark shift for the dark excitons.

II. THEORETICAL MODEL

We use an ab-initio-based tight-binding Hamiltonian that allows us to reproduce the single-particle band structure obtained by density functional theory (DFT). The linearized augmented plane wave code WIEN2K⁶⁴ is used employing the exchange-correlation functional PBE⁶⁵ to compute the DFT band structure of MoS₂ with a lattice constant of 3.14 Å.⁶⁶ Then, the Wannierization is carried out with a 12×12 uniform sampling of the Brillouin zone using the WANNIER90 package.⁶⁷ Depending on whether SOC is taken into account, a linear combination of S-centered *p*- and Mo-centered *d*-orbitals is chosen to project onto the separated manifold of either five (no SOC) or ten (SOC) bands in the low-energy region. The spreads of the maximally localized Wannier functions are smaller than 5 Å².

A given single-particle state $|n\mathbf{k}\rangle$ with the 2D wave vector \mathbf{k} in band *n* and energy $\epsilon_{n\mathbf{k}}$ can then be written as the Bloch sum

$$|n\mathbf{k}\rangle = \frac{1}{\sqrt{N}} \sum_{\nu,i} e^{i\mathbf{k}\cdot\mathbf{R}_i} a_{n\mathbf{k}\nu} |\nu, \mathbf{R}_i\rangle, \quad (1)$$

where $|\nu, \mathbf{R}_i\rangle$ is the Wannier orbital ν centered at the Bravais lattice point \mathbf{R}_i and *N* is the total number of primitive unit cells considered. The coefficients $a_{n\mathbf{k}\nu}$ are determined from the tight-binding Hamiltonian $\mathcal{H}_{\nu\nu'}(\mathbf{k})$ via $\sum_{\nu'} \mathcal{H}_{\nu\nu'}(\mathbf{k}) a_{n\mathbf{k}\nu'} = \epsilon_{n\mathbf{k}} a_{n\mathbf{k}\nu}$. Throughout this manuscript, we will label conduction and valence band indices by $n = c$ and $n = v$.

In the absence of an electric field, we employ the procedure described in Ref. 68 to compute excitons *S* with momentum $q_{\text{exc}} = 0$ and solve the Bethe-Salpeter equation

(BSE),

$$\Delta_{v\mathbf{c}\mathbf{k}} A_{v\mathbf{c}\mathbf{k}}^S + \sum_{v'c'\mathbf{k}'} \mathcal{K}_{v\mathbf{c}\mathbf{k},v'c'\mathbf{k}'} A_{v'c'\mathbf{k}'}^S = \Omega_S A_{v\mathbf{c}\mathbf{k}}^S. \quad (2)$$

Here, Ω_S denotes the energy of the exciton state $|\Psi_S\rangle = \sum_{v\mathbf{c}\mathbf{k}} A_{v\mathbf{c}\mathbf{k}}^S \hat{c}_{c\mathbf{k}}^\dagger \hat{c}_{v\mathbf{k}} |\text{GS}\rangle$ with the coefficients $A_{v\mathbf{c}\mathbf{k}}^S$, the creation (annihilation) operator of an electron with momentum \mathbf{k} in a conduction band *c* (valence band *v*) $\hat{c}_{c\mathbf{k}}^\dagger$ ($\hat{c}_{v\mathbf{k}}$), and the ground state $|\text{GS}\rangle$ with fully occupied valence bands and unoccupied conduction bands. The BSE is governed by the energy difference $\Delta_{v\mathbf{c}\mathbf{k}} = \epsilon_{c\mathbf{k}} - \epsilon_{v\mathbf{k}}$ between the non-interacting states $|c\mathbf{k}\rangle$ and $|v\mathbf{k}\rangle$ and the interaction kernel

$$\mathcal{K}_{v\mathbf{c}\mathbf{k},v'c'\mathbf{k}'} = \mathcal{K}_{v\mathbf{c}\mathbf{k},v'c'\mathbf{k}'}^{\text{d}} + \mathcal{K}_{v\mathbf{c}\mathbf{k},v'c'\mathbf{k}'}^{\text{x}}, \quad (3)$$

which consists of the direct and exchange terms, $\mathcal{K}_{v\mathbf{c}\mathbf{k},v'c'\mathbf{k}'}^{\text{d}}$ and $\mathcal{K}_{v\mathbf{c}\mathbf{k},v'c'\mathbf{k}'}^{\text{x}}$.⁶⁹

We model the interaction in $\mathcal{K}_{v\mathbf{c}\mathbf{k},v'c'\mathbf{k}'}^{\text{d}}$ by the screened Coulomb interaction in a 2D insulator,^{33,70}

$$W(|\mathbf{R}_{ij}^{\nu\nu'}|) = \frac{e^2}{8\epsilon_0 r_0} \left[H_0 \left(\frac{\varepsilon |\mathbf{R}_{ij}^{\nu\nu'}|}{r_0} \right) - Y_0 \left(\frac{\varepsilon |\mathbf{R}_{ij}^{\nu\nu'}|}{r_0} \right) \right], \quad (4)$$

where H_0 and Y_0 are the Struve function and the Bessel function of the second kind. Here, $\mathbf{R}_{ij}^{\nu\nu'} = \mathbf{R}_{ij} + \boldsymbol{\tau}_\nu - \boldsymbol{\tau}_{\nu'}$, where $\mathbf{R}_{ij} = \mathbf{R}_i - \mathbf{R}_j$ and $\boldsymbol{\tau}_\nu$ and $\boldsymbol{\tau}_{\nu'}$ denote the centers of the Wannier orbitals ν and ν' in the primitive unit cell as computed by WANNIER90. The length $r_0 = 2\pi\chi_{2\text{D}}$ is related to the 2D polarizability $\chi_{2\text{D}}$,³³ $e = |e|$ is the absolute value of the electron charge, and ϵ_0 and ε are the vacuum permittivity and the background dielectric constant. The background dielectric constant is given by $\varepsilon = (\varepsilon_1 + \varepsilon_2)/2$, where $\varepsilon_{1,2}$ denotes the dielectric constants of the materials above and below the MoS₂ layer. This potential has proven highly successful in capturing excitonic properties of TMDs.³³

Assuming point-like Wannier orbitals,

$$\begin{aligned} \mathcal{K}_{v\mathbf{c}\mathbf{k},v'c'\mathbf{k}'}^{\text{d}} = & - \sum_{\nu\nu'} a_{c\mathbf{k}\nu}^* a_{c'\mathbf{k}'\nu} a_{v\mathbf{k}\nu'} a_{v'\mathbf{k}'\nu'}^* \\ & \times \left[\frac{1}{N^2} \sum_{i,j} e^{-i(\mathbf{k}-\mathbf{k}')\cdot\mathbf{R}_{ij}} W(|\mathbf{R}_{ij}^{\nu\nu'}|) \right] \end{aligned} \quad (5)$$

and

$$\begin{aligned} \mathcal{K}_{v\mathbf{c}\mathbf{k},v'c'\mathbf{k}'}^{\text{x}} = & \sum_{\nu\nu'} a_{c\mathbf{k}\nu}^* a_{v\mathbf{k}\nu} a_{c'\mathbf{k}'\nu'} a_{v'\mathbf{k}'\nu'}^* \\ & \times \left[\frac{1}{N^2} \sum_{i,j} V(|\mathbf{R}_{ij}^{\nu\nu'}|) \right] \end{aligned} \quad (6)$$

are computed in real space with the screened interaction (4) and the bare Coulomb interaction $V(|\mathbf{R}_{ij}^{\nu\nu'}|) = e^2/(4\pi\epsilon_0\varepsilon|\mathbf{R}_{ij}^{\nu\nu'}|)$, respectively.⁷¹ An electric field *F* along

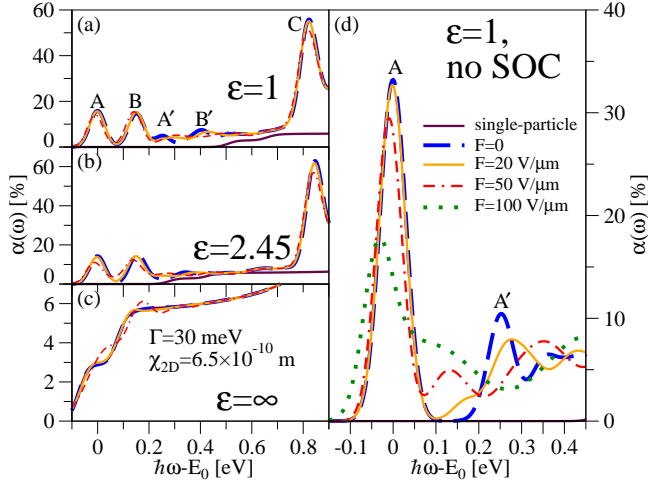


FIG. 2. (Color online) Calculated absorption spectra of monolayer MoS₂ for several different dielectric environments, (a) $\epsilon = 1$, (b) $\epsilon = 2.45$, and (c) $\epsilon = \infty$, measured from the absorption onset E_0 .^a (d) Same as in panel (a), but without SOC. We use $\chi_{2D} = 6.5 \text{ \AA}$ and a Gaussian broadening of $\Gamma = 30 \text{ meV}$.

^a In experiments, $E_0 \approx 1.9 \text{ eV}$. Here, we apply a rigid shift to the band structure obtained from our DFT-based tight-binding model to describe the quasiparticle band gap as obtained by GW.

the (Bravais) unit direction \mathbf{e}_1 is accounted for by including the potential

$$U_F(\mathbf{R}_{ij}^{\nu\nu'}) = eF\mathbf{R}_{ij}^{\nu\nu'} \cdot \mathbf{e}_1 \times \tanh \left\{ k_0 \left[\frac{1}{4} - \left(\frac{\mathbf{R}_{ij}^{\nu\nu'} \cdot \mathbf{e}_1}{L} \right)^2 \right] \right\}, \quad (7)$$

and adding it to $W(|\mathbf{R}_{ij}^{\nu\nu'}|)$ in Eq. (5).⁵⁸ To avoid numerical instabilities, the potential (7) contains a smoothing factor, where L is the length of the super cell along the \mathbf{e}_1 -direction. The parameter k_0 controls how fast the electrostatic potential decays at the edge of the super cell. A general in-plane field \mathbf{F} can be considered by decomposing the field as $\mathbf{F} = F_1\mathbf{e}_1 + F_2\mathbf{e}_2$ and adding Eq. (7) for each direction to $W(|\mathbf{R}_{ij}^{\nu\nu'}|)$ in Eq. (5). Since in our calculations we find that the Stark effect on the main exciton absorption peaks is not sensitive to the direction of the in-plane field, we restrict ourselves to a field along the \mathbf{e}_1 -direction and Eq. (7).

The exciton states obtained from Eq. (2) can be used to compute the absorbance

$$\alpha(\omega) = \frac{e^2\pi}{\epsilon_0 c \omega} \frac{1}{A} \sum_S \left| \sum_{\mathbf{c}\mathbf{k}} A_{\mathbf{v}\mathbf{c}\mathbf{k}}^S d_{\mathbf{v}\mathbf{c}}(\mathbf{k}) \right|^2 \delta(\hbar\omega - \Omega_S) \quad (8)$$

of a 2D sheet with unit area A . Here, we have introduced the photon energy $\hbar\omega$, the single-particle/quasiparticle dipole-matrix element $d_{\mathbf{v}\mathbf{c}}(\mathbf{k}) = \sum_{\nu, \nu'} a_{\mathbf{v}\mathbf{k}\nu}^* a_{\mathbf{c}\mathbf{k}\nu'} \partial_{k_x} \mathcal{H}_{\nu\nu'}(\mathbf{k})/\hbar$ obtained from the tight-binding model for the transition between states $|\mathbf{c}\mathbf{k}\rangle$ and

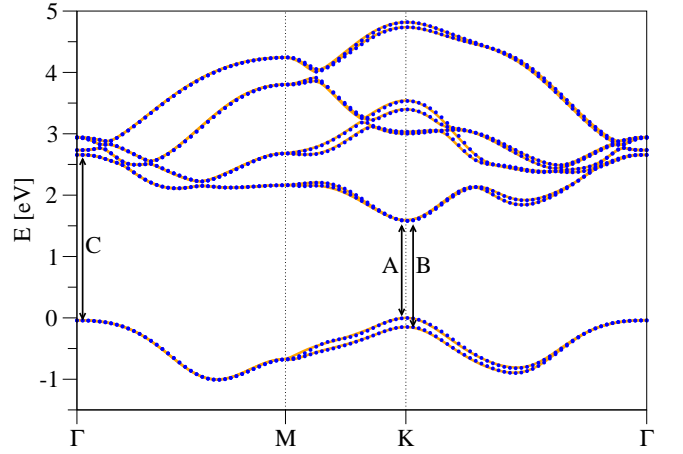


FIG. 3. (Color online) Band structure of monolayer MoS₂ as obtained from DFT (orange lines) and as calculated using an ab-initio-based tight-binding model (blue circles) with SOC. The optical transitions involving the A and B excitons at the K (K') point and the C exciton near the Γ point are also marked.

$|\mathbf{v}\mathbf{k}\rangle$, and the velocity of light c . Since the gap between the conduction and valence bands is much larger than the spin-orbit splitting, we compute the excitons using the single-particle band structure without SOC and following Ref. 34 employ first-order perturbation theory to include SOC near the K and K' points.⁷² Unless explicitly stated otherwise, our calculations are performed on a 144×144 k -grid/super cell with an upper energy cut-off of 2 eV above the band gap. This ensures that the exciton binding energies presented in this work are converged with a relative error of less than 10^{-5} when going from a 132×132 k -grid to a 144×144 k -grid. We have set the smoothing parameter $k_0 = 10$ throughout the manuscript and checked that the results are not affected for the fields presented in this work if larger values for k_0 are used ($k_0 = 20$, $k_0 = 30$, and $k_0 = 50$).

III. RESULTS

To illustrate the effect of an electric field, Fig. 2 displays the absorption spectra of ML MoS₂ for several different dielectric environments. For clarity, we also show the behavior of the lowest exciton peaks for $\epsilon = 1$ in the absence of SOC in Fig. 2 (d). At zero field and $\epsilon = 1$, one can clearly see the A and B exciton peaks originating from transitions into the spin-orbit-split valence bands at the K and K' points, their respective Rydberg states, A' and B' , as well as the so-called C exciton that arises due to transitions near the Γ point [see Fig. 2 (a)]. The origin of these excitons is also depicted in Fig. 3, which shows the band structure of ML MoS₂ obtained from our tight-binding description. Moreover, a comparison with the original DFT band structure illustrates an almost perfect agreement between the two band structures.

χ_{2D} [\AA]	ε	E_b [meV]	κ [(eV $\mu\text{m}/\text{V}$) ²]	$\tilde{\alpha}$ [eV $\mu\text{m}^2/\text{V}^2$]	λ [($\mu\text{m}/\text{V}$) ²]
5.0	1	603	2.43×10^{-6}	8.06×10^{-6}	2.99×10^{-5}
6.5	1	508	2.75×10^{-6}	1.08×10^{-5}	5.37×10^{-5}
6.5	2.45	279	2.28×10^{-6}	1.63×10^{-5}	1.20×10^{-4}
6.5	3.35	214	2.40×10^{-6}	2.24×10^{-5}	1.87×10^{-4}
6.5	5	143	2.53×10^{-6}	3.54×10^{-5}	4.21×10^{-4}

TABLE I. Binding energies E_b , fitting parameters κ with corresponding electric polarizabilities $\tilde{\alpha}$ in Eq. (9), and λ in Eq. (10) for different dielectric environments ε and χ_{2D} .

Due to the screened potential given by Eq. (4) we obtain a nonhydrogenic Rydberg series for the A and B excitons, a fact well established experimentally⁴² and theoretically.^{33,34,39} Depending on the value of χ_{2D} as given in the literature,³³ our model predicts binding energies E_b of around 500-600 meV for the A and B excitons at $\varepsilon = 1$ (see also Table I). As ε is increased, the binding energies of the A , B , and C excitons decrease, which can be seen in Fig. 2 (b), where we have chosen $\varepsilon = (1 + 3.9)/2 = 2.45$ to model the dielectric environment of MoS₂ on a SiO₂ substrate.

If an electric field is applied, the binding energies of the A , B , and C excitons increase by $\delta E_b(F) =$

$E_b(F) - E_b(F = 0)$ due to the Stark effect. Their peaks, on the other hand, lose spectral weight, a part of which is transferred into the region between the A/B exciton peaks and the onset of the continuum. At high fields an additional absorption peak arises in this region, while the continuum absorption exhibits Franz-Keldysh oscillations [see Figs. 2 (a), (b) and (d)]. The period of these oscillations is proportional to the electric field and their amplitude also grows with increasing field, which is corroborated in Fig. 2 (c), where — in the absence of any electron-hole interaction, $\varepsilon = \infty$, and consequently excitons — the electric field leads only to Franz-Keldysh modulations of the absorption.⁵⁶

The Stark shift δE_b of the lowest excitonic states depends on E_b at zero field as shown in Fig. 4 (a). For fields up to 20 V/ μm , we find Stark shifts of the order of several meV, similar to the optical Stark shifts observed recently in WSe₂,⁶² while the shift is much larger for $F = 50$ V/ μm [see Figs. 2 (a), (b) and (d)], for example, $\delta E_b \approx 10$ meV for free standing MoS₂ ($\varepsilon = 1$), $\delta E_b \approx 17$ meV for MoS₂ on SiO₂ ($\varepsilon = 2.45$), and $\delta E_b \approx 18$ meV for MoS₂ on diamond [$\varepsilon = (1 + 5.7)/2 = 3.35$]. Figure 2 (d) implies that for $\varepsilon \approx 1$ the exciton peak can still be observed at $F = 100$ V/ μm with a Stark shift of $\delta E_b \approx 32$ meV. At low fields and high binding energies, δE_b can be fitted very well to a quadratic function

$$\delta E_b = \tilde{\alpha} F^2 / 2 = \kappa F^2 / E_b, \quad (9)$$

where the fitting parameter κ is related to the electric polarizability $\tilde{\alpha} = 2\kappa/E_b$ and found to be around $\kappa \approx 2.5 \times 10^{-6}$ (eV $\mu\text{m}/\text{V}$)², nearly independent of ε and χ_{2D} , with the actual values obtained for best fits given in Table I. Equation (9) is motivated by the form of the second-order correction due to the Stark effect in the hydrogen atom and the small exciton radius. Since our calculations point to κ being only weakly dependent on the dielectric background and the polarizabilities, Eq. (9) implies that E_b in different dielectric setups can be obtained by fitting the quadratic field dependence of the Stark shift to a constant inversely proportional to E_b . Figure 4 (a) also illustrates that for high fields and low binding energies, such as for $\varepsilon = 5$, δE_b deviates from

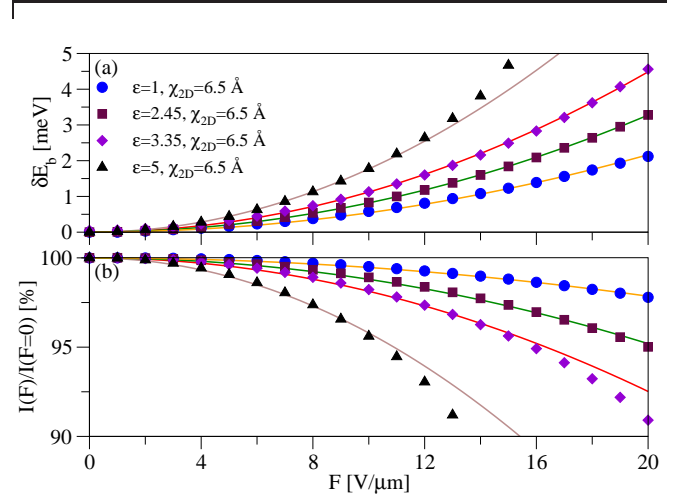


FIG. 4. (Color online) Field dependence of (a) the Stark shifts δE_b and (b) the relative oscillator strengths $I(F)/I(F = 0)$ of the lowest excitons for different dielectric environments. Symbols denote computed data points, whereas the solid lines denote best fits given by Eqs. (9) and (10) and Table I.

this quadratic behavior and higher order corrections in F become more important.

Moreover, we study the loss of the spectral weight of the exciton peaks with increasing F . Figure 4 (b) displays the oscillator strengths $I(F)$ [normalized to the oscillator strength at $F = 0$, $I(F = 0)$] of the lowest exciton

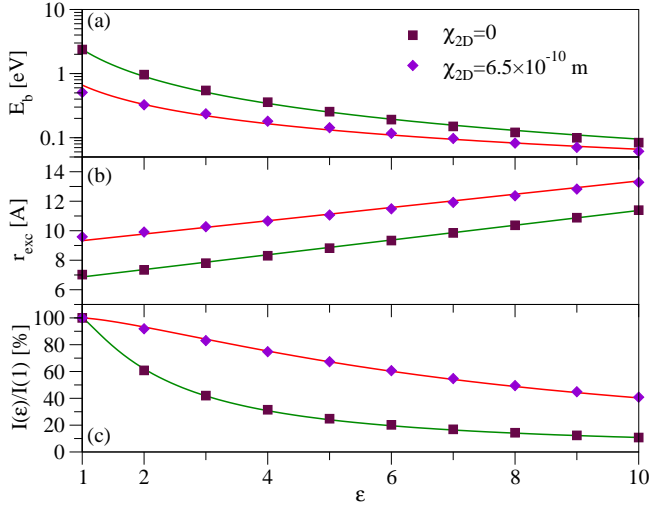


FIG. 5. (Color online) Dependence of (a) the binding energy E_b , (b) the exciton radius r_{exc} , and (c) the relative oscillator strengths $I(\epsilon)/I(\epsilon = 1)$ of the lowest excitons at $F = 0$. Symbols denote computed data points, whereas the solid lines denote best fits to a power law in panel (a), to a linear dependence in panel (b), and to Eq. (11) in panel (c).

peak, for which we find that its field dependence can be approximated by

$$\frac{I(F)}{I(F=0)} = 1 - \lambda F^2. \quad (10)$$

Table I gives values of the parameter λ , which varies widely for different combinations of χ_{2D} and ϵ and cannot be easily related to E_b .

An electric field is expected to decrease the exciton lifetime leading to a broadening of the exciton absorption peak due to the exciton dissociation. These effects can be related to the loss of spectral weight displayed in Fig. 4 (b). Since this loss is quite small for typical values of ϵ , around 5% for $\epsilon = 2.45$ and $F = 20$ V/ μ m, Fig. 4 (b) implies that the A and B exciton peaks require very large fields beyond which they fully dissociate. This in turn suggests that one should be able to observe an excitonic Stark effect in MoS₂ MLs experimentally. The Rydberg states A' and B' , on the other hand, dissociate already at smaller fields due to their lower binding energy as shown in Fig. 2.

As we have shown in Fig. 4, the Stark shifts strongly depend on the binding energy at zero field. Hence, we study the dependence of E_b of the lowest exciton on the dielectric environment in Fig. 5, where we compare the results obtained for the screened potential with $\chi_{2D} = 6.5$ Å with those of the bare Coulomb potential (with $\chi_{2D} = 0$). Figure 5 (a) illustrates that the dependence of E_b on ϵ can be reasonably well fitted to power laws, $E_b \propto \epsilon^{-1.4}$ for $\chi_{2D} = 0$ and $E_b \propto \epsilon^{-1}$ for $\chi_{2D} = 6.5$ Å, which differ from the hydrogen model for the range of ϵ in Fig. 5. This is due to two reasons: (i) The discreteness of the Bravais lattice results in deviations from the

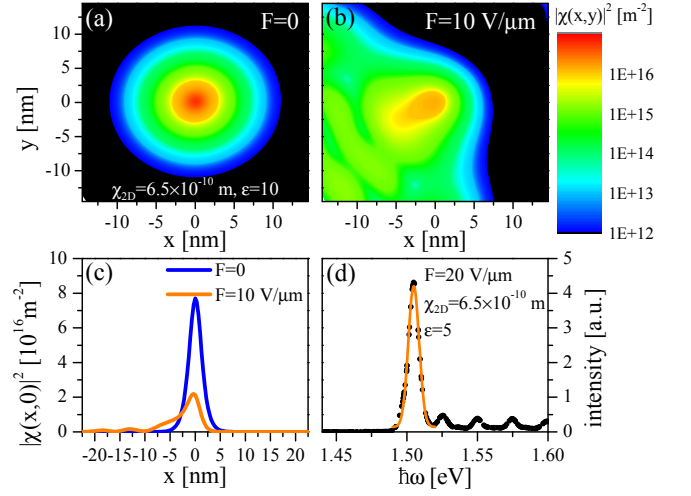


FIG. 6. (Color online) Density plots of the exciton wave function $|\chi(x,y)|^2$ for $\epsilon = 10$ and $\chi_{2D} = 6.5$ Å at (a) $F = 0$ and (b) $F = 10$ V/ μ m in x -direction. Panel (c) compares the x -dependence of $|\chi(x,y)|^2$ at $y = 0$ for $F = 0$ and $F = 10$ V/ μ m as shown in panels (a) and (b). (d) Optical transition intensities and Gaussian fit of the line shape for $\epsilon = 5$, $\chi_{2D} = 6.5$ Å, and $F = 20$ V/ μ m.

continuum model of the hydrogen atom, which predicts the binding energy to scale as $E_b \propto \epsilon^{-2}$. (ii) For finite χ_{2D} , the potential deviates from the bare Coulomb potential at short distances $r \rightarrow 0$, which is particularly relevant for small exciton radii r_{exc} and, hence, small ϵ . As we increase ϵ , r_{exc} becomes larger compared to the lattice constant and exponents closer to the hydrogen model are found, $E_b \propto \epsilon^{-1.7}$ and $E_b \propto \epsilon^{-1.5}$ for the bare and screened potentials, respectively, using a range of ϵ from 10 to 20 (not shown).

The corresponding exciton radii r_{exc} of the lowest excitons are displayed in Fig. 5 (b). One can see that r_{exc} , although increasing with ϵ , does not change significantly for typical values of ϵ , by at most 10% for $\epsilon = 5$. Figure 5 (c) shows the oscillator strengths $I(\epsilon)$ of the exciton peak normalized to its value at $\epsilon = 1$. With increasing ϵ , the spatial overlap of the electron and hole wave functions and, hence, $I(\epsilon)$ are diminished as expected. In both cases, $\chi_{2D} = 0$ and $\chi_{2D} = 6.5$ Å, its behavior scales with the exciton radius r_{exc} as

$$I(\epsilon) = \beta / [r_{exc}(\epsilon) - R_0]^2 \quad (11)$$

with the proportionality constant $\beta \approx 7.1 \times 10^{-9}$ m⁴/s² and a length scale $R_0 \approx |\mathbf{a}_{1/2}| = 3.1$ Å on the order of the lattice constant.

Figure 6 compares the amplitudes of the wave function⁷³ $|\chi(x,y)|^2$ computed from the BSE for $\epsilon = 10$ and $\chi_{2D} = 6.5$ Å at zero field [Fig. 5 (a)] and $F = 10$ V/ μ m [Fig. 5 (b)]. By fitting $|\chi(x,y)|^2$ to a Gaussian, we find a Bohr radius of around 13 Å for the exciton from Figs. 6 (a) and (c) [also shown in Fig. 5 (b)], comparable to the length scales reported in the literature.³⁸ If an electric field is applied, the wave function leaks out of

χ_{2D} [Å]	ε	$E_b^{2p,l}$ [meV]	$\kappa_{2p,l}$ [(eV $\mu\text{m}/\text{V}$) ²]	$\tilde{\alpha}_{2p,l}$ [eV $\mu\text{m}^2/\text{V}^2$]	$E_b^{2p,u}$ [meV]	$\kappa_{2p,u}$ [(eV $\mu\text{m}/\text{V}$) ²]	$\tilde{\alpha}_{2p,u}$ [eV $\mu\text{m}^2/\text{V}^2$]
6.5	1	334	6.17×10^{-6}	3.69×10^{-5}	312	1.14×10^{-5}	7.31×10^{-5}
6.5	2.45	138	9.90×10^{-6}	1.43×10^{-4}	126	1.33×10^{-5}	2.12×10^{-4}
6.5	3.35	97	1.59×10^{-5}	3.27×10^{-4}	83	1.61×10^{-5}	3.88×10^{-4}
6.5	5	49	2.59×10^{-5}	1.07×10^{-3}	45	2.00×10^{-5}	8.95×10^{-4}

TABLE II. Binding energies $E_b^{2p,l}$ and $E_b^{2p,u}$ as well as fitting parameters $\kappa_{2p,l}$ and $\kappa_{2p,u}$ in Eq. (9) with corresponding electric polarizabilities $\tilde{\alpha}_{2p,l}$ and $\tilde{\alpha}_{2p,u}$ of the lower (l) and upper (u) $2p$ exciton states for the dielectric environments used in Fig. 7.

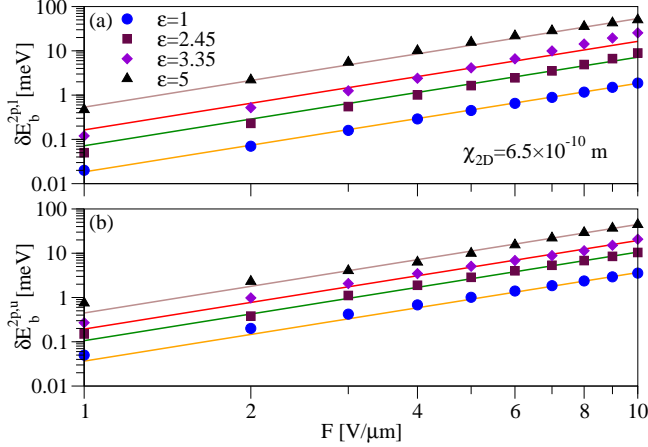


FIG. 7. (Color online) Field dependence of the Stark shifts of the (a) lower and (b) upper $2p$ exciton states, $\delta E_b^{2p,l}$ and $\delta E_b^{2p,u}$, for different dielectric environments. Symbols denote computed data points, whereas the solid lines denote fits to Eq. (9) and Table II.

the central region [see Figs. 6 (b) and (c)]. This leakage can be used to calculate the tunneling probability of an exciton into the free electron-hole continuum, which can in turn be related to the exciton dissociation rate.⁵⁸

For high electric fields and/or relatively small binding energies, the exciton ionization lifetime can also be determined as follows: While an exciton and its peak at zero field corresponds to one single solution of the BSE (2), this single solution splits into several eigenstates of the

BSE at finite electric field. The distribution of these split peaks, an example of which is shown in Fig. 6 (d), determines the intrinsic linewidth, which we find from a Gaussian fit. We use a 240×240 k -mesh to obtain the spectrum in Fig. 6 (d) using a Gaussian broadening of $\Gamma_e = 3$ meV. The broadening Γ from the fit in Fig. 6 (d) is due to the convolution of the intrinsic ionization decay rate Γ_i and an extrinsic broadening Γ_e , such that $\Gamma = \sqrt{\Gamma_e^2 + \Gamma_i^2}$. In this way, we obtain a lifetime broadening of $\Gamma_i \approx 2.4$ meV or 2.7×10^{-13} s for $E_b = 143$ meV, in good agreement with recent calculations⁷⁴ and experimental data in WSe₂.⁵⁰ These very short exciton decay lifetimes imply a rapid field-induced dissociation into free carriers that in turn can potentially contribute to photoconductivity⁷⁵ and be used in photodetectors^{7,76} or solar cells.⁹

Until now, we have only considered bright excitons that appear in the linear optical absorption as displayed in Fig. 2. Labeling the excitons in analogy to the hydrogen series, the A/B and A'/B' excitons correspond to $1s$ and $2s$ states, respectively. In contrast, excitons with finite orbital angular momentum are dipole-forbidden and do not contribute to the linear absorption, but can be probed by two-photon absorption measurements.⁵⁰ Consistent with recent theoretical predictions,^{39,77} we find that at zero field the $2p$ states are more strongly bound than the $2s$ state. Moreover, the two $2p$ states (per valley) are not degenerate, but split by 22 meV for $\varepsilon = 1$. The upper $2p$ state, that is, the $2p$ state with lower binding energy, is in turn 56 meV below the $2s$ state for $\varepsilon = 1$.

Figure 7 displays the Stark shifts $E_b^{2p,l}$ and $E_b^{2p,u}$ of the lower [Fig. 7 (a)] and upper [Fig. 7 (b)] $2p$ states for different dielectric environments. Similarly to the s -like A/B and A'/B' excitons, the Stark shift increases with ε , that is, with decreasing binding energy of the $2p$ states. Moreover, for both $2p$ states, we find $\delta E_b^{2p,l/u}$ to be of the order of tens of meV, and thus typically larger than δE_b for the A and B peaks, due to their smaller binding energies [see Table II]. At small fields or large binding energies $E_b^{2p,l/u}$, we can fit $\delta E_b^{2p,l/u}$ to Eq. (9), where we substitute E_b by $E_b^{2p,l/u}$ and summarize the

fitting parameters in Table II. This nonlinear behavior of $\delta E_b^{2p,l/u}$ is a consequence of the broken degeneracy of the $2p$ states and provides another striking difference of the excitonic series in TMDs compared to the hydrogen series.

IV. CONCLUSIONS

We have theoretically investigated excitons and the absorption spectra of MoS₂ monolayers in the presence of

an applied in-plane electric field using a tight-binding and many-body Bethe-Salpeter-equation approach. Our calculations predict a quadratic Stark shift for the main exciton peaks in the linear absorption spectra, which is of the order of a few meV for fields of 10 V/ μm and can exceed 30 meV for a larger electric field of 100 V/ μm . Moreover, the loss of oscillator strength with the field and the scaling with the binding energy and the dielectric environment have been investigated. Our results imply that very large fields are required beyond which these excitons fully dissociate into free electron-hole pairs. In addition, we have found subpicosecond exciton field ionization lifetimes at fields of a few tens of V/ μm , which could be utilized in solar energy harvesting and photodetection. Finally, we have investigated the Stark effect not only on bright excitons that appear in the linear absorption, but also on the dark $2p$ excitons. For those excitons, we predict a Stark shift of the order of tens of meV, and

thus typically larger than the shift of the main absorption peaks. Remarkably, we predict the $2p$ excitons to also exhibit a nonlinear scaling, in contrast to the linear Stark effect of p states in the hydrogen atom. While we have focused on MoS₂, our findings suggest that a versatile engineering of the electro-optical response should be possible in other transition metal dichalcogenide monolayers as well.

ACKNOWLEDGMENTS

We gratefully acknowledge Rupert Huber and Yang-Fang Chen for stimulating discussions and suggestions. This work was supported by U.S. DOE, Office of Science BES, under Award de-sc0004890 (I.Ž.), by U.S. ONR N000141310754 (B.S.), and by DFG Grants No. SCHA 1899/1-1 (B.S.), No. GRK 1570 (T.F., J.F.) and No. SFB 689 (M.G., J.F.).

-
- * bscharf@buffalo.edu
† zigor@buffalo.edu
‡ v.perebeinos@skoltech.ru
- ¹ R. A. Bromley, R. B. Murray, and A. D. Yoffe, *Journal of Physics C: Solid State Physics* **5**, 759 (1972).
 - ² K. F. Mak, C. Lee, J. Hone, J. Shan, and T. F. Heinz, *Phys. Rev. Lett.* **105**, 136805 (2010).
 - ³ Q. H. Wang, K. Kalantar-Zadeh, A. Kis, J. N. Coleman, and M. S. Strano, *Nat. Nanotechnol.* **7**, 699 (2012).
 - ⁴ A. Kormányos, G. Burkard, M. Gmitra, J. Fabian, V. Zólyomi, N. D. Drummond, and V. Falko, *2D Mater.* **2**, 022001 (2015).
 - ⁵ D. Lembke and A. Kis, *ACS Nano* **6**, 10070 (2012).
 - ⁶ W. Bao, X. Cai, D. Kim, K. Sridhara, and M. S. Fuhrer, *Appl. Phys. Lett.* **102**, 042104 (2013).
 - ⁷ O. Lopez-Sanchez, D. Lembke, M. Kayci, A. Radenovic, and A. Kis, *Nat. Nanotechnol.* **8**, 497 (2013).
 - ⁸ L. Britnell, R. M. Ribeiro, A. Eckmann, R. Jalil, B. D. Belle, A. Mishchenko, Y.-J. Kim, R. V. Gorbachev, T. Georgiou, S. V. Morozov, A. N. Grigorenko, A. K. Geim, C. Casiraghi, A. H. C. Neto, and K. S. Novoselov, *Science* **340**, 1311 (2013).
 - ⁹ A. Pospischil, M. M. Furchi, and T. Mueller, *Nat. Nanotechnol.* **9**, 257 (2014).
 - ¹⁰ X. Yin, Z. Ye, D. A. Chenet, Y. Ye, K. O'Brien, J. C. Hone, and X. Zhang, *Science* **344**, 488 (2014).
 - ¹¹ F. Wang, P. Stepanov, M. Gray, and C. N. Lau, *Nanotechnology* **26**, 105709 (2015).
 - ¹² X. Cui, G.-H. Lee, Y. D. Kim, G. Arefe, P. Y. Huang, C.-H. Lee, D. A. Chenet, X. Zhang, L. Wang, F. Ye, F. Pizzocchero, B. S. Jessen, K. Watanabe, T. Taniguchi, D. A. Muller, T. Low, P. Kim, and J. Hone, *Nat. Nanotechnol.* **10**, 534 (2015).
 - ¹³ S. Rath, I. Lee, D. Lim, J. Wang, Y. Ochiai, N. Aoki, K. Watanabe, T. Taniguchi, G.-H. Lee, Y.-J. Yu, P. Kim, and G.-H. Kim, *Nano Lett.* **15**, 5017 (2015).
 - ¹⁴ D. Dumcenco, D. Ovchinnikov, K. Marinov, P. Lazic, M. Gibertini, N. Marzari, O. L. Sanchez, Y.-C. Kung, D. Krasnozhan, M.-W. Chen, S. Bertolazzi, P. Gillet, A. F. i Morral, A. Radenovic, and A. Kis, *ACS Nano* **9**, 4611 (2015).
 - ¹⁵ D. Xiao, G.-B. Liu, W. Feng, X. Xu, and W. Yao, *Phys. Rev. Lett.* **108**, 196802 (2012).
 - ¹⁶ T. Cao, G. Wang, W. Han, H. Ye, C. Zhu, J. Shi, Q. Niu, P. Tan, E. Wang, B. Liu, and J. Feng, *Nat. Commun.* **3**, 887 (2012).
 - ¹⁷ H. Zeng, J. Dai, W. Yao, D. Xiao, and X. Cui, *Nat. Nanotechnol.* **7**, 490 (2012).
 - ¹⁸ K. F. Mak, K. He, J. Shan, and T. F. Heinz, *Nat. Nanotechnol.* **7**, 494 (2012).
 - ¹⁹ K. F. Mak, K. L. McGill, J. Park, and P. L. McEuen, *Science* **344**, 1489 (2014).
 - ²⁰ A. Srivastava, M. Sidler, A. V. Allain, D. S. Lembke, A. Kis, and A. Imamoglu, *Nat. Phys.* **11**, 141 (2015).
 - ²¹ A. V. Stier, K. M. McCreary, B. T. Jonker, J. Kono, and S. A. Crooker, *Nat. Commun.* **7**, 10643 (2016).
 - ²² T. Scrase, Y. Tsai, B. Barman, L. Schweidenback, A. Petrou, G. Kioseoglou, I. Ozfidan, M. Korkusinski, and P. Hawrylak, *Nat. Nanotechnol.* **10**, 603 (2015).
 - ²³ A. Splendiani, L. Sun, Y. Zhang, T. Li, J. Kim, C.-Y. Chim, G. Galli, and F. Wang, *Nano Lett.* **10**, 1271 (2010).
 - ²⁴ M. Amani, D.-H. Lien, D. Kiriya, J. Xiao, A. Azcatl, J. Noh, S. R. Madhupathy, R. Addou, S. KC, M. Dubey, K. Cho, R. M. Wallace, S.-C. Lee, J.-H. He, J. W. Ager, X. Zhang, E. Yablonovitch, and A. Javey, *Science* **350**, 1065 (2015).
 - ²⁵ I. Žutić, J. Fabian, and S. Das Sarma, *Rev. Mod. Phys.* **76**, 323 (2004); J. Fabian, A. Matos-Abiague, C. Ertler, P. Stano, and I. Žutić, *Acta Phys. Slov.* **57**, 565 (2007).
 - ²⁶ Y. Song and H. Dery, *Phys. Rev. Lett.* **111**, 026601 (2013).
 - ²⁷ L. Yang, N. A. Sinitsyn, W. Chen, J. Yuan, J. Zhang, J. Lou, and S. A. Crooker, *Nat. Phys.* **11**, 830 (2015).
 - ²⁸ J. Lee, S. Bearden, E. Wasner, and I. Žutić, *Appl. Phys. Lett.* **105**, 042411 (2014).
 - ²⁹ M. Gmitra and J. Fabian, *Phys. Rev. B* **92**, 155403 (2015).

- ³⁰ T. Cheiwchanchamnangij and W. R. L. Lambrecht, Phys. Rev. B **85**, 205302 (2012).
- ³¹ A. Ramasubramaniam, Phys. Rev. B **86**, 115409 (2012).
- ³² H. Shi, H. Pan, Y.-W. Zhang, and B. I. Yakobson, Phys. Rev. B **87**, 155304 (2013).
- ³³ T. C. Berkelbach, M. S. Hybertsen, and D. R. Reichman, Phys. Rev. B **88**, 045318 (2013).
- ³⁴ D. Y. Qiu, F. H. da Jornada, and S. G. Louie, Phys. Rev. Lett. **111**, 216805 (2013).
- ³⁵ H.-P. Komsa and A. V. Krashennnikov, Phys. Rev. B **88**, 085318 (2013).
- ³⁶ A. Molina-Sánchez, D. Sangalli, K. Hummer, A. Marini, and L. Wirtz, Phys. Rev. B **88**, 045412 (2013).
- ³⁷ A. Steinhoff, M. Rösner, F. Jahnke, T. O. Wehling, and C. Gies, Nano Lett. **14**, 3743 (2014).
- ³⁸ C. Zhang, H. Wang, W. Chan, C. Manolatu, and F. Rana, Phys. Rev. B **89**, 205436 (2014).
- ³⁹ F. Wu, F. Qu, and A. H. MacDonald, Phys. Rev. B **91**, 075310 (2015).
- ⁴⁰ T. Stroucken and S. W. Koch, J. Phys.: Condens. Matter **27**, 345003 (2015).
- ⁴¹ H. Dery and Y. Song, Phys. Rev. B **92**, 125431 (2015).
- ⁴² A. Chernikov, T. C. Berkelbach, H. M. Hill, A. Rigosi, Y. Li, O. B. Aslan, D. R. Reichman, M. S. Hybertsen, and T. F. Heinz, Phys. Rev. Lett. **113**, 076802 (2014).
- ⁴³ A. Chernikov, A. M. van der Zande, H. M. Hill, A. F. Rigosi, A. Velauthapillai, J. Hone, and T. F. Heinz, Phys. Rev. Lett. **115**, 126802 (2015).
- ⁴⁴ K. He, N. Kumar, L. Zhao, Z. Wang, K. F. Mak, H. Zhao, and J. Shan, Phys. Rev. Lett. **113**, 026803 (2014).
- ⁴⁵ G. Wang, X. Marie, I. Gerber, T. Amand, D. Lagarde, L. Bouet, M. Vidal, A. Balocchi, and B. Urbaszek, Phys. Rev. Lett. **114**, 097403 (2015).
- ⁴⁶ M. M. Ugeda, A. J. Bradley, S.-F. Shi, F. H. da Jornada, Y. Zhang, D. Y. Qiu, W. Ruan, S.-K. Mo, Z. Hussain, Z.-X. Shen, F. Wang, S. G. Louie, and M. F. Crommie, Nat. Mater. **13**, 1091 (2014).
- ⁴⁷ Z. Ye, T. Cao, K. O'Brien, H. Zhu, X. Yin, Y. Wang, S. G. Louie, and X. Zhang, Nature **513**, 214 (2014).
- ⁴⁸ B. Zhu, X. Chen, and X. Cui, Scientific Reports **5**, 9218 (2015).
- ⁴⁹ A. Hanbicki, M. Currie, G. Kioseoglou, A. Friedman, and B. Jonker, Solid State Commun. **203**, 16 (2015).
- ⁵⁰ C. Poellmann, P. Steinleitner, U. Leierseder, P. Nagler, G. Plechinger, M. Porer, R. Bratschitsch, C. Schüller, T. Korn, and R. Huber, Nat. Mater. **14**, 889 (2015).
- ⁵¹ K. F. Mak, K. He, C. Lee, G. H. Lee, J. Hone, T. F. Heinz, and J. Shan, Nat. Mater. **12**, 207 (2013).
- ⁵² J. S. Ross, S. Wu, H. Yu, N. J. Ghimire, A. M. Jones, G. Aivazian, J. Yan, D. G. Mandrus, D. Xiao, W. Yao, and X. Xu, Nat. Commun. **4**, 1474 (2013).
- ⁵³ B. Ganchev, N. Drummond, I. Aleiner, and V. Fal'ko, Phys. Rev. Lett. **114**, 107401 (2015).
- ⁵⁴ M. M. Fogler, L. V. Butov, and K. S. Novoselov, Nat. Commun. **5**, 4555 (2014).
- ⁵⁵ E. V. Calman, C. J. Dorow, M. M. Fogler, L. V. Butov, S. Hu, A. Mishchenko, and A. K. Geim, ArXiv 1510.04410.
- ⁵⁶ W. Franz, Z. Naturforsch. **13A**, 484 (1958); L. V. Keldysh, Zh. Eksp. Teor. Fiz. **34**, 1138 (1958), [Sov. Phys.—JETP **7**, 788 (1958)].
- ⁵⁷ D. A. B. Miller, D. S. Chemla, T. C. Damen, A. C. Gosard, W. Wiegmann, T. H. Wood, and C. A. Burrus, Phys. Rev. Lett. **53**, 2173 (1984); Y.-H. Kuo, Y. K. Lee, Y. Ge, S. Ren, J. E. Roth, T. I. Kamins, D. A. B. Miller, and J. S. Harris, Nature **437**, 1334 (2005).
- ⁵⁸ V. Perebeinos and P. Avouris, Nano Lett. **7**, 609 (2007).
- ⁵⁹ A. Chaves, T. Low, P. Avouris, D. Çakir, and F. M. Peeters, Phys. Rev. B **91**, 155311 (2015).
- ⁶⁰ F. Withers, O. D. Pozo-Zamudio, S. Schwarz, S. Dufferwiel, P. M. Walker, T. Godde, A. P. Rooney, A. Gholinia, C. R. Woods, P. Blake, S. J. Haigh, K. Watanabe, T. Taniguchi, I. L. Aleiner, A. K. Geim, V. I. Falko, A. I. Tartakovskii, and K. S. Novoselov, Nano Lett. **15**, 8223 (2015).
- ⁶¹ J. Klein, J. Wierzbowski, A. Regler, J. Becker, F. Heimbach, K. Müller, M. Kaniber, and J. J. Finley, Nano Lett. **16**, 1554 (2016).
- ⁶² J. Kim, X. Hong, C. Jin, S.-F. Shi, C.-Y. S. Chang, M.-H. Chiu, L.-J. Li, and F. Wang, Science **346**, 1205 (2014).
- ⁶³ E. J. Sie, J. W. McIver, Y.-H. Lee, L. Fu, J. Kong, and N. Gedik, Nat. Mater. **14**, 290 (2015).
- ⁶⁴ P. Blaha, K. Schwarz, G. K. H. Madsen, D. Kvasnicka, and J. Luitz, *WIEN2k, An Augmented Plane Wave+Local Orbitals Program for Calculating Crystal Properties*, edited by K. Schwarz, Vol. 1 (Technische Universität Wien, Austria, 2001).
- ⁶⁵ J. P. Perdew, K. Burke, and M. Ernzerhof, Phys. Rev. Lett. **77**, 3865 (1996).
- ⁶⁶ The energy cutoff is set to an equivalent of 150 eV to ensure converged results. Self-consistent calculations are done at a k -sampling of 30×30 .
- ⁶⁷ N. Marzari and D. Vanderbilt, Phys. Rev. B **56**, 12847 (1997).
- ⁶⁸ M. Rohlfing and S. G. Louie, Phys. Rev. B **62**, 4927 (2000).
- ⁶⁹ If the non-interacting quasiparticle states are spin-degenerate, the exciton states can be categorized as singlet and triplet states, whose BSE (2) is calculated only from the real-space quasiparticle wave functions and contains the kernels $\mathcal{K} = \mathcal{K}^d + 2\mathcal{K}^x$ and $\mathcal{K} = \mathcal{K}^d$, respectively.
- ⁷⁰ L. V. Keldysh, Pis'ma Zh. Eksp. Teor. Fiz. **29**, 716 (1979), [JETP Lett. **29**, 658 (1979)]; P. Cudazzo, I. V. Tokatly, and A. Rubio, Phys. Rev. B **84**, 085406 (2011).
- ⁷¹ We omit terms with $R_{ij}^{\nu\nu'} = 0$.
- ⁷² Spin-orbit coupling is included by comparing the ab-initio band structures with and without SOC, adding their band- and \mathbf{k} -dependent energy differences as a perturbation to the BSE, and calculating the corresponding corrections in first-order perturbation theory.
- ⁷³ In order to determine the exciton wave function, we compute the pair correlation function using the solution of the BSE (2).
- ⁷⁴ H. Wang, C. Zhang, W. Chan, C. Manolatu, S. Tiwari, and F. Rana, Phys. Rev. B **93**, 045407 (2016).
- ⁷⁵ M. M. Furchi, D. K. Polyushkin, A. Pospischil, and T. Mueller, Nano Lett. **14**, 6165 (2014).
- ⁷⁶ F. H. L. Koppens, T. Mueller, P. Avouris, A. C. Ferrari, M. S. Vitiello, and M. Polini, Nat. Nanotechnol. **9**, 780 (2014).
- ⁷⁷ T. C. Berkelbach, M. S. Hybertsen, and D. R. Reichman, Phys. Rev. B **92**, 085413 (2015).